Nano Research

Open Access

Research Article

Oxygen vacancies-rich TiO_{2-x} enhanced composite polyurethane electrolytes for high-voltage solid-state lithium metal batteries

Xiaoning Xu[1,2], Fei Pei[1] ✉, Wenjie Lin[1], Jia Lei[1], Yuhan Yang[1], Henghui Xu[1], Zhen Li[1] ✉, and Yunhui Huang[1]

[1] *State Key Laboratory of Materials Processing and Die & Mould Technology, School of Materials Science and Engineering, Huazhong University of Science and Technology, Wuhan 430074, China*
[2] *Dongfeng Motor Corporation Research & Development Institute, Wuhan 430058, China*

Cite this article: *Nano Research*, **2025**, *18*, 94907304. https://doi.org/10.26599/NR.2025.94907304

ABSTRACT: Due to the favorable interfacial stability with electrodes, excellent processability, and reasonable material cost, organic–inorganic composite solid-state electrolytes have attracted broad interests in the field of solid-state batteries. In this study, we have developed a solid-state composite electrolyte with polyurethane (PU) as polymer matrix and TiO_{2-x} as nanofiller (denoted as PUL-TiO_{2-x}). The block copolymer PU features alternating soft and hard segments, which offers distinct advantages due to its unique structural arrangement. The soft segment of the block copolymer facilitates the dissociation of lithium salt, enabling the conduction of Li^+, while the rich hydrogen bond network formed by the hard segment ensures the mechanical strength of the electrolyte. The profusion of Lewis acid sites on the TiO_{2-x} surface facilitates interactions with ether oxygen groups and bistrifluoromethanesulfonimide ($TFSI^-$) anions, thereby enhancing ionic conductivity (σ) and expanding the electrochemical stability window of the electrolyte. Notably, the PUL-TiO_{2-x} electrolyte exhibits an impressive σ of 2.19 × 10^{-4} S·cm^{-1} at 40 °C, a Li^+ transference number of 0.47, and an electrochemical stability window of 4.98 V. The resulting $LiNi_{0.8}Co_{0.1}Mn_{0.1}O_2$ (NCM811)||Li battery demonstrates a specific capacity of 171 mAh·g^{-1} and exhibits excellent cycling stability, maintaining its performance over 270 cycles at 40 °C. These findings underscore the immense potential of the PUL-TiO_{2-x} in advancing the development of high-performance all-solid-state lithium batteries.

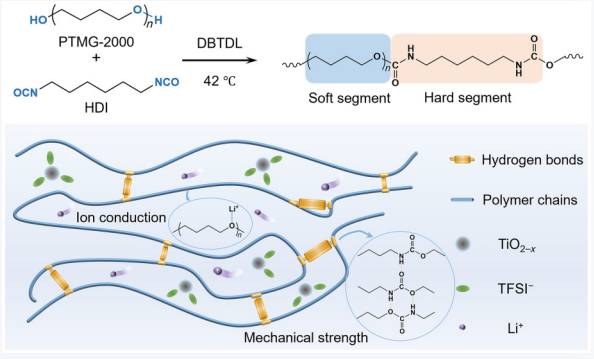

KEYWORDS: polyurethane electrolyte, composite polymer electrolytes, high-voltage cathodes, solid-state lithium metal batteries

1 Introduction

Lithium-ion batteries have already achieved widespread usage in various fields, such as portable electronics and electric vehicles [1]. However, the ongoing development of lithium-ion batteries faces significant challenges to increase the energy density and maintain high safety at the same time [2–5]. By replacing liquid electrolytes with solid-state electrolytes (SSEs), the risk of leaks and flammability can be mitigated, minimizing the potential for combustion and explosions in extreme conditions [6, 7]. Moreover, SSEs offer superior mechanical properties, making them highly compatible with lithium metal anodes to achieve high energy density [8]. Thus, developing suitable SSEs stands as a crucial aspect in the progress of all-solid-state lithium-metal batteries (ASSLBs) [9, 10].

Among various solid-state electrolyte choices, solid-state polymer electrolytes (SPEs) offer excellent flexibility, enabling improved interface contact, and facilitating ease of processing and preparation [11, 12]. These qualities make SPEs highly conducive to large-scale industrial production, aligning with the demands of the lithium battery market. However, SPEs still have several challenges to overcome, such as low ionic conductivity (σ) at room temperature, poor mechanical strength, and inadequate electrochemical stability [13, 14]. Various methods, including designing polymer matrices [15, 16], incorporating plasticizers [17], and integrating ceramic fillers [18–21], have been explored to enhance the properties of SPEs. Notably, the macromolecular design with multiple functional groups offers a promising avenue for fundamentally altering the electrochemical and mechanical characteristics of the electrolytes

Received: November 26, 2024; **Revised:** February 5, 2025
Accepted: February 13, 2025

✉Address correspondence to Fei Pei, peifei@hust.edu.cn; Zhen Li, li_zhen@hust.edu.cn

[22, 23]. Furthermore, the integration of ceramic fillers into the polymer matrix holds immense potential in achieving superior composite solid polymer electrolytes (CSPEs) [24, 25]. By judiciously selecting and incorporating ceramic fillers, it becomes possible to augment the ionic conductivity, expand the electrochemical potential window, and enhance the overall mechanical strength of the electrolyte [26, 27]. While numerous studies have explored the use of TiO_2 as a commonly employed nano-filler, scant attention has been given to the influence of oxygen vacancies on the TiO_2 surface and their impact on ion conduction and electrochemical stability [28, 29]. Further exploration of the role of oxygen vacancies presents a promising avenue to enhance the electrochemical performance of CSPEs [30].

In this study, we have developed an all-solid-state composite electrolyte with polyurethane (PU) as polymer matrix and TiO_{2-x} as nanofiller. The PU utilized in our study is a block copolymer featuring alternating soft and hard segments, in which the soft segment facilitates the dissociation of lithium salt, enabling the conduction of Li^+ ions, while the rich hydrogen bond network formed by the hard segment ensures the mechanical strength of the electrolyte. The profusion of Lewis acid sites on the TiO_{2-x} surface facilitates interactions with ether oxygen groups and bistrifluoromethanesulfonimide ($TFSI^-$) anions, thereby enhancing ionic conductivity and expanding the electrochemical stability window. As a result, the synthesized composite solid-state electrolyte demonstrates an impressive ionic conductivity of 2.19×10^{-4} S·cm^{-1} at 40 °C, coupled with an extended electrochemical stability window of 4.98 V. These remarkable properties enable the stable cycling of $LiNi_{0.8}Co_{0.1}Mn_{0.1}O_2$ (NCM811)||Li solid-state lithium batteries.

2 Experimental

2.1 Materials

Polytetramethylene ether glycol (PTMG, the number-average molecular weight (M_n) = 2000), hexamethylene diisocyanate (HDI, 99%), dibutyltin dilaurate (DBTDL, 95%), dichloromethane (CH_2Cl_2, 99.5%), methanol (99.5%), N,N-dimethylacetamide (DMAc, 98%), bistrifluoromethanesulfonimide lithium salt (LiTFSI, 99%), deuterated chloroform ($CDCl_3$, 99.8%), tetrahydrofuran (THF, analytical reagent (AR)), N-methylpyrrolidone (NMP, 99.5%), titanium dioxide (TiO_2, 25 nm), and other chemicals and solvents were analytical reagents and require no further purification.

2.2 Preparation of TiO_{2-x}

The pristine TiO_2 nanoparticles were reduced in H_2 atmosphere (5% H_2 and 95% Ar) at 400 °C for 2 h (heating rate: 5 °C·min^{-1}). The obtained TiO_{2-x} products were dispersed in the DMAc by ultrasound for 0.5 h.

2.3 Synthesis of polyurethane-based electrolytes

PTMG (1.0 g, 0.50 mmol) was heated and dissolved in 2 mL CH_2Cl_2, followed by the addition of HDI (90 μL, 0.56 mmol) and initiator DBTDL (one drop). The mixture was stirred at 42 °C for different amounts of time (4, 5, and 6 h) and 6 mL of DMAc was added dropwise. Finally, methanol was added to seal the ends. For electrolytes containing nanofillers, the nanofillers TiO_2 or TiO_{2-x} (0.055 g, 5 wt.%) need to be ultrasonically dispersed in 6 mL DMAc by ultrasonic homogenizer and subsequently dropped into the mixture. The optimized mass of LiTFSI (0.498 g, the molar ratio of ethylene oxide (EO) to Li (EO:Li) = 8:1) was added to the mixed solution and stirred to dissolve thoroughly. When a homogeneous solution was obtained, it was poured on the Teflon mold or electrode and dried at 60 °C for 12 h to remove the solvent. The obtained PU electrolytes after adding the LiTFSI were denoted as PUL, PUL-TiO_2, and PUL-TiO_{2-x}, respectively. The thickness of the resulting films was about 50–100 μm. Furthermore, the films employed in the tests without lithium salt were denoted as PU and PU-TiO_{2-x}.

2.4 Electrode preparation and cell assembly

The $LiFePO_4$ (LFP) and NCM811 cathodes were prepared by casting a viscous slurry containing LFP or NCM811, poly(vinyl difluoride) (PVDF) binder, and Super P carbon with a weight ratio of 8:1:1 in NMP onto a carbon-coated aluminum foil. The electrodes were then dried under vacuum at 80 °C for 12 h. The areal mass loading of the LFP and NCM811 active material in the cathodes were 5 and 2 mg·cm^{-2}, respectively.

CR2032-type cells were assembled to evaluate the cycling stability and rate performance. The electrolyte was coated onto the surfaces of the anode and cathode, followed by drying at 60 °C for 12 h to achieve excellent interfacial contact. The solid-state Li-metal batteries were assembled by attaching the cathode and Li anode covered with electrolyte in an argon-filled glove box. For the batteries with NCM811 cathode, both the charge–discharge and cycling properties were evaluated between 3.0 and 4.3 V with an automatic galvanostatic charge–discharge unit (GCD, Neware) at 40 °C.

2.5 Electrochemical tests

The electrochemical impedance spectroscopy (EIS, from 30 to 80 °C) of the stainless steel (SS) models was applied to evaluate the σ and activation energy (E_a) [31]. The frequency of the EIS test was from 1 to 10^6 Hz with a 5 mV amplitude. We calculated σ according to Eq. (1)

$$\sigma = \frac{l}{R_b A} \tag{1}$$

where R_b is bulk resistance. l and A are the thickness and area of the electrolytes, respectively. We used the Vogel–Tammann–Fulcher (VTF) equation, as shown in Eq. (2), to calculate E_a

$$\sigma = \sigma_0 T^{-\frac{1}{2}} \exp\left(\frac{-E_a}{R(T-T_0)}\right) \tag{2}$$

where σ_0 is the frequency factor. T is the absolute temperature. R is the molar gas constant. T_0 is normally called the equilibrium glass-transition temperature (around glass transition temperature (T_g) – 50 K) [32].

The Li^+ transference number (t_{Li^+}) of the electrolyte was calculated by a combination measurement of alternating current (AC) impedance and potentiostatic direct current (DC) polarization. A DC voltage of 10 mV was applied to the Li||Li symmetrical battery, and the EIS of the battery before and after DC polarization were measured in the frequency range from 1 to 10^6 Hz. The t_{Li^+} was then calculated using Eq. (3)

$$t_{Li^+} = \frac{I_{SS}(\Delta V - I_0 R_0)}{I_0(\Delta V - I_{SS} R_{SS})} \tag{3}$$

where ΔV is the polarization voltage. I_0 and I_{SS} are the initial current and steady-state current. R_0 and R_{SS} are the interface impedance

before and after DC polarization. A similar method was used for electronic conductivity testing with a DC polarization of 1 V [33].

The electrochemical stability windows of the electrolytes were evaluated by linear sweep voltammetry (LSV) curves of Li||SS cells with a scan rate of 1 mV·s^{-1}.

2.6 Characterization

The proton nuclear magnetic resonance (^{1}H NMR) analysis was performed on a NMR spectrometer AscendTM 600 MHz (Bruker) using $CDCl_3$ as the solvent. Fourier transform infrared (FTIR) spectroscopy was measured using a Nicolet iS50R (Thermo Scientific) with a diamond attenuated total reflectance (ATR) attachment. Differential scanning calorimetry (DSC) measurements were performed using instrument DSC2500 (TA Instruments) with a heating rate of 10 °C·min^{-1} from −90 to 120 °C under a nitrogen atmosphere. Thermogravimetric (TG) analysis was performed using instrument TGA8000 (PerkinElmer) at a heating rate of 10 °C·min^{-1} from room temperature to 700 °C. Mechanical tensile-stress experiments were performed using instrument Instron-5944 with a tensile rate of 30 mm·min^{-1}. The X-ray powder diffraction (XRD) pattern was recorded by X'Pert^3 powder (PANalytical B.V.) diffractometer, and the radiation source was Cu K_α (λ = 0.154 nm). Scanning electron microscope (SEM) images were taken on the Nova Nano SEM 450 (FEI) field emission SEM. Gel permeation chromatography (GPC) was performed in THF using PL-GPC50 (Agilent). Electron paramagnetic resonance (EPR) spectra of samples were collected on an EMXmicro spectrometer (Bruker).

3 Results and discussion

3.1 Synthesis and characterization of polyurethane

As depicted in Fig. 1(a), the synthesis of PU macromolecules involves the reaction between a highly unsaturated group isocyanate group and a hydroxyl group containing active hydrogen. The working principle of the PUL-TiO_{2-x} is illustrated in Fig. 1(b). PU incorporates a soft segment based on the ionic conductive polymer PTMG, which exhibits a lower spatial density of ether-oxygen groups compared to polyethylene oxide (PEO). This property facilitates the loose coordination between the ether-oxygen groups and lithium ions [34–36]. The inclusion of HDI as a hard segment in the polymer structure facilitates the formation of a robust hydrogen bond network, which contributes significantly to the mechanical strength of the material [37]. Moreover, the presence of hydrogen bonding enhances PU's self-healing ability and adhesion characteristics, resulting in excellent interface compatibility and safety performance [32, 38].

The successful synthesis of the PU molecule was confirmed by the ^{1}H NMR analysis, as shown in Fig. S1 in the Electronic Supplementary Material (ESM). In the FTIR spectrum (Fig. 1(c)), the absorption band observed at 3319 cm^{-1} corresponds to the stretching vibration of the hydrogen-bonded N–H group. Notably, no absorption peaks were observed at 3450 and 2270 cm^{-1}, indicating the absence of –OH and –NCO groups, respectively, thereby confirming the successful reaction between the PTMG monomer and HDI [35, 39, 40]. The stretching vibration of the C=O group was observed as two distinct peaks at 1721 and 1686 cm^{-1}, representing the free C=O and hydrogen-bonded C=O, respectively. The blue shift is attributed to the formation of strong hydrogen bonds between the –NH–COO– groups. Similarly, the stretching vibration of the C–N group exhibited two characteristic peaks at 1537 and 1446 cm^{-1}, corresponding to the hydrogen-bonded C–N and free C–N, respectively [41]. These observations signify the presence of numerous hydrogen bond interactions within and between PU molecules, contributing to the favorable mechanical properties and self-healing ability of the polymer.

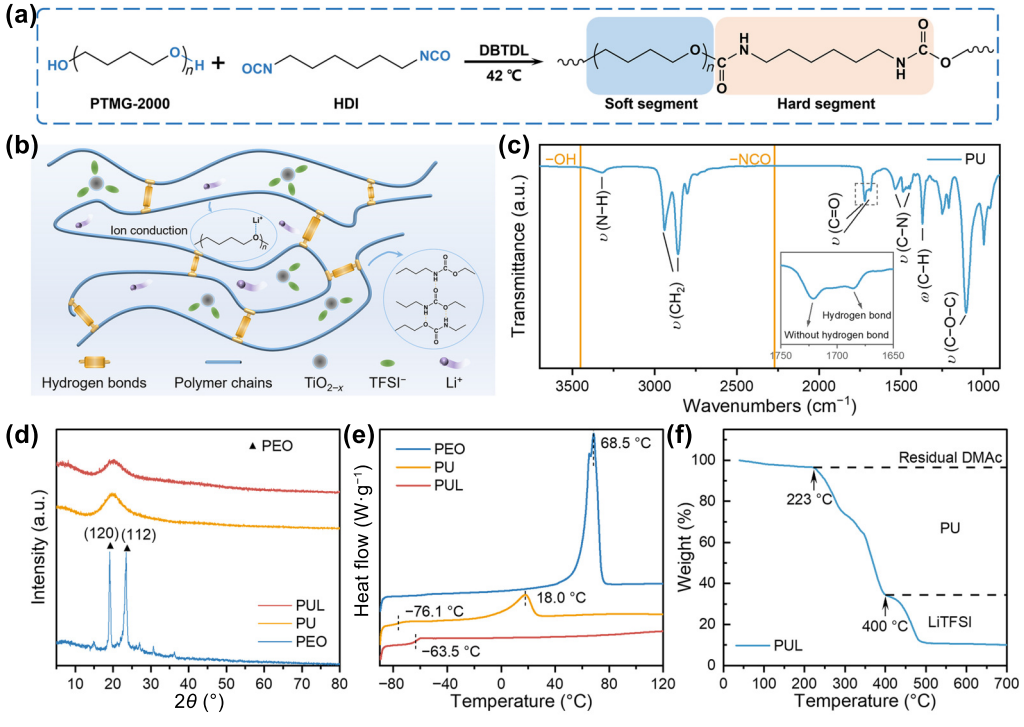

Figure 1 Schematic and characterization of the PU macromolecules. (a) Synthesis and chemical structures of PU. (b) Schematic illustration of ion transport and hydrogen-bonding reinforcement in PUL-TiO_{2-x}. (c) FTIR spectra of PU. (d) The XRD patterns and (e) the DSC curves for PEO, PU, and PUL. (f) TG curves of PUL under a N_2 atmosphere.

XRD measurements were performed to investigate the structural and crystalline properties of the polymer. As shown in Fig. 1(d), PU exhibited a dispersed diffraction peak at 19.8°, suggesting its amorphous nature at room temperature. Upon the addition of lithium salt to obtain PUL, the diffraction peak further broadened, indicating a reduction in the crystallinity of PU. The crystallization behavior was further investigated using DSC. Figure 1(e) illustrates that PEO displayed a melting endothermic peak around 68.5 °C, while the melting point of PU was significantly lower at 18.0 °C. Moreover, PU exhibited a T_g of only −76.1 °C, signifying its semi-crystalline structure. Conversely, no melting peak was observed in PUL, indicating its amorphous nature. The observed small crystalline region in PU indicates enhanced mobility of polymer chain segments, facilitating faster transport of lithium ions. The thermal stability of the solid electrolyte is a paramount factor that must be carefully considered to guarantee the utmost level of safety and reliability in battery systems. In Fig. 1(f), the TG curve illustrates a negligible weight loss below 223 °C, which signifies the exceptional thermal stability of PUL.

3.2 Characterization of PU with different molecular weight

The thermal shrinkage test was employed to evaluate the morphological stability of the polymer at elevated temperatures (Fig. 2(a)) [42]. The Celgard separator exhibits minor shrinkage below 120 °C, while significant deformation occurs at 140 °C, compromising its effectiveness in maintaining proper separation between the cathodes and anodes. PEO displayed evident melting behavior at 160 °C, signifying a transition into a viscous flow state, which limits its ability to suppress the growth of lithium dendrites. In contrast, both PU and PU-TiO_{2-x} films displayed minimal changes in size and state even at elevated temperatures of 160 °C, highlighting the thermal stability improvement attributed to the rich hydrogen bond network within the polymer and the incorporation of inorganic particles.

PUs with varying molecular weights (PU-1, PU-2, and PU-3) were synthesized by meticulously controlling the polymerization time for 4, 5, and 6 h. Subsequently, the synthesized PUs were subjected to GPC analysis for molecular weight characterization. The results of Table S1 in the ESM indicate a sequential increase in molecular weights from PU-1 to PU-3.

Optical photos of the tensile test of PU-1 are shown in Fig. 2(b). The mechanical properties of PUs with different molecular weights were assessed through stress–strain curve analysis. In Fig. 2(c), PU-1 exhibited a low tensile strength (1.74 MPa) and the highest elongation at break (1636%), indicating a viscous liquid-like mechanical state lacking sufficient rigidity. With an increase in the main chain, the stress required to deform the PU increased while the elongation at break decreased. Notably, PU-2 and PU-3 demonstrated tensile strengths of 6.89 and 20.52 MPa, and elongations at break of 1506% and 1436%, respectively. The improved mechanical strength and elasticity can be attributed to the microphase separation structure [43]. The presence of hydrogen bonds between the hard segments acts as physical anchors, offering support during the stretching of the polymer electrolyte film. Simultaneously, the soft segments polyether undergo extension, leading to an increased elongation at break. The increase in molecular weight contributes to enhanced intermolecular and intramolecular hydrogen bond crosslinking. The dynamic nature of hydrogen bonds strengthens the interactions between polymer chains, consequently improving the overall mechanical properties.

To further assess the performance of solid electrolytes prepared using PU with varying molecular weights, Li|SPEs|Li symmetrical batteries were assembled. Figure 2(d) shows that PUL-1 has the lowest polarization voltage of only 82.7 mV at low current density. However, at higher current density and lithium deposition, PUL-1 demonstrates pronounced voltage fluctuations, indicating its limited mechanical properties in inhibiting lithium dendrite growth and leading to battery failure caused by short circuit. In contrast, the voltage curves of PUL-2 and PUL-3 remain stable throughout the cycling process, suggesting a more uniform plating and stripping of lithium metal. The stability observed can be attributed to the electrolyte's exceptional mechanical strength, which effectively suppresses dendrite growth under such conditions.

The polarization voltages of PUL-3 (151.6 and 305.7 mV) are slightly higher than those of PUL-2 (130.1 and 248.1 mV). This can

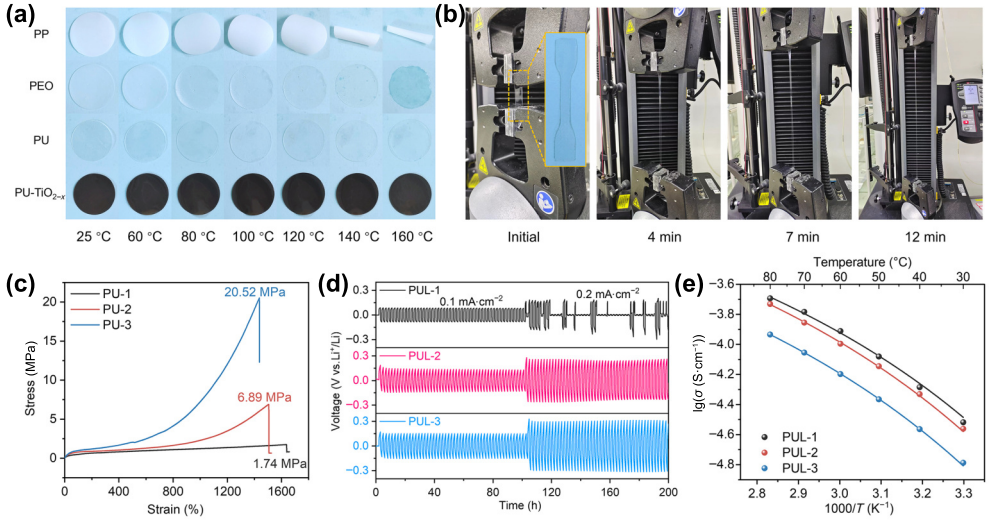

Figure 2 Characterization of mechanical and electrochemical properties of PUs with different molecular weights. (a) Optical photographs of thermal shrinkage tests of Celgard, PEO, PU, and PU-TiO_{2-x} at different temperatures for 30 min. (b) Optical photos of stress–strain test of PU-2. (c) Stress–strain curves of PU-1 to PU-3 at an extension rate of 30 mm·min^{-1}. (d) Voltage profiles of long-term lithium plating/stripping cycles in a 2 h period for Li||Li symmetric cells assembled from PUL-1 to PUL-3 at the current densities of 0.1 and 0.2 mA·cm^{-2} at 40 °C. (e) Temperature dependence of the ionic conductivities of PUL-1, PUL-2, and PUL-3.

be attributed to the lower ionic conductivity of PUL-3. The presence of a rich hydrogen bond network enhances the mechanical properties of the polymer, but simultaneously restricts the movement of chain segments, thereby reducing the rate of lithium-ion conduction. Consequently, as molecular weight increases, the polymer's mechanical strength improves while the ionic conductivity of the corresponding electrolyte decreases. PUL-2, with a moderate degree of polymerization, strikes a balance between ionic conductivity and mechanical strength, making it more suitable for battery applications (Fig. 2(e) and Table S2 in the ESM). The subsequent synthesis of PU is performed by following the specifications of PU-2 as the reference.

3.3 Preparation and characterization of composite electrolyte

The incorporation of inorganic fillers into the polymer matrix for electrolyte modification has emerged as a prominent research area in recent years. This approach offers several advantages. Firstly, the presence of inorganic fillers disrupts the regular crystalline structure of the polymer, leading to increased amorphous content and improved chain segment mobility. Secondly, the Lewis acid-base interaction between the filler surface, polymer molecules, and lithium salts facilitates the formation of a rapid ion transport pathway at the organic/inorganic interface layer. Moreover, it expands the electrochemical stability window of the electrolyte and promotes the dissociation of Li^+ ions [19, 44].

Black TiO_{2-x} nanoparticles, distinguished by the presence of oxygen vacancies, were prepared via hydrogen reduction of TiO_2, with Fig. S2(a) in the ESM depicting their optical photograph. Figure S2(b) in the ESM displays a transmission electron microscope (TEM) image of TiO_{2-x}, with 55 individual particles selected and measured to construct the particle size distribution diagram for TiO_{2-x} particles (Fig. S2(c) in the ESM). These results indicate that the average particle size of TiO_{2-x} is 26 nm. Figure S3 in the ESM displays inorganic particles with a scale bar of 10 nm, revealing the presence of an amorphous layer around the edges of the TiO_{2-x} particles. This layer is a product of the reduction reaction and may contribute to the superior performance of the electrolyte. The presence of oxygen vacancies in TiO_{2-x} was confirmed through EPR. As shown in Fig. 3(a), a prominent peak at the vacancy with a g value of 2.003 indicates the abundance of oxygen vacancies in the material [45]. The ultrasonic crushing process effectively dispersed the nanoparticles in the solvent, and the inorganic particles within the electrolyte maintained excellent dispersion (Fig. S4 in the ESM). SEM images of the electrolyte (Fig. S5 in the ESM) revealed a uniform and dense film without noticeable holes or cracks. Additionally, the elemental mapping of Ti confirmed the uniform distribution of TiO_{2-x} nanoparticles within the electrolyte. The XRD patterns in Fig. S6 in the ESM reveal that the peaks observed in PUL-TiO_2 and PUL-TiO_{2-x} are in good agreement with the standard pattern of anatase TiO_2.

The influence of TiO_{2-x} on the ionic conductivity of the composite electrolyte was investigated by conducting impedance tests on SS||SS batteries (Figs. 3(b) and 3(c) and Table S3 in the ESM). The measured conductivity values at 40 °C were 4.67×10^{-5}, 1.63×10^{-4}, and 2.19×10^{-4} S·cm^{-1} for PUL, PUL-TiO_2, and PUL-TiO_{2-x}, respectively. The results indicate that the incorporation of inorganic fillers results in the physical degradation of the polymer chain structure and a reduction in crystallinity. Additionally, the presence of abundant Lewis acid sites on the TiO_{2-x} surface facilitates interactions with ether oxygen groups, establishing efficient ion transport pathways at the organic/inorganic interface. The temperature-dependent behavior of ionic conductivity was successfully described using the VTF empirical equation, exhibiting a high correlation coefficient close to 1. The activation energy values for PUL-TiO_{2-x} (3.8 kJ·mol^{-1}) were lower compared to those of PUL-TiO_2 (4.0 kJ·mol^{-1}) and PUL (4.4 kJ·mol^{-1}), indicating enhanced lithium-ion migration in the PUL-TiO_{2-x} electrolyte resulting from improved polymer chain mobility and the creation of efficient ion transport channels. The ideal composite solid electrolyte requires

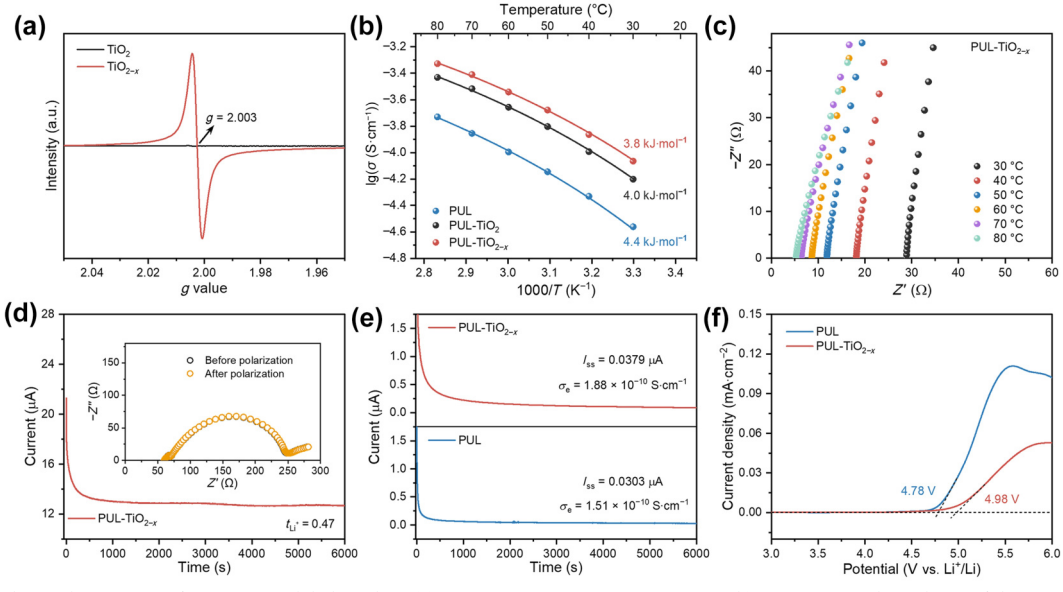

Figure 3 Electrochemical properties of composite solid electrolyte. (a) EPR to measure oxygen vacancies. (b) Temperature dependence of the ionic conductivities of PUL, PUL-TiO_2, and PUL-TiO_{2-x}. The symbols are experimental data, and the solid lines are VTF fitting results for ionic conductivities of the elastomeric polymer electrolytes. (c) Nyquist plots of PUL-TiO_{2-x} electrolyte from 30 to 80 °C. (d) The chronoamperometry curves of PUL-TiO_{2-x} at a potential step of 10 mV at 40 °C. The inset figure shows AC impedance spectra of the same cell before and after polarization. (e) Electronic conductivities of PUL and PUL-TiO_{2-x} at a voltage of 1 V at 40 °C. (f) LSV of PUL and PUL-TiO_{2-x} at 40 °C.

high ionic conductivity and low electronic conductivity. The Li||Li battery was examined using chronoamperometry and AC impedance techniques [33]. As shown in Fig. 3(d) and Fig. S7 in the ESM, the calculated lithium-ion transference number of PUL-TiO_{2-x} was 0.47, higher than that of PUL-TiO_2 (0.36) and PUL (0.24). This increase in t_{Li^+} can be attributed to the presence of abundant positively charged oxygen vacancies on the surface of TiO_{2-x}, which strongly interact with $TFSI^-$ in the electrolyte, leading to the release of more Li^+ ions. High electronic conductivity is a major factor contributing to the growth of lithium dendrites in solid electrolytes. To evaluate the electronic conductivity of the electrolyte, a SS||SS battery was assembled, and the DC polarization method was employed for measurement. The results depicted in Fig. 3(e) reveal that the electronic conductivity is in the order of 10^{-10} S·cm^{-1}, suggesting that the electron transfer can be considered negligible.

In order to achieve higher energy density, it is crucial for the electrolyte to be compatible with high-voltage cathodes. The oxidation stability of PUL and PUL-TiO_{2-x} were assessed using LSV measurements conducted on Li||SS cells. The introduction of a more stable $-CH_3$ terminal group during polymerization enhances the high voltage stability of the polymer [46]. Figure 3(f) illustrates the calculation of the electrolyte's oxidation stability by determining the tangent of the decomposition curve and the intercept of the baseline. The electrochemical stability window of PUL is measured at 4.78 V, while that of PUL-TiO_{2-x} is further increased to 4.98 V. We speculate that the Lewis acid sites on the surface of TiO_{2-x} interact with the ether-oxygen structure, potentially providing protection against oxidative decomposition.

3.4 Electrochemical characterization of the SPEs

Fig. 4(a) illustrates the FTIR spectra in the range of 1400–1150 cm^{-1}, along with the corresponding Gaussian–Lorentz fitting results. Indeed, the observed shift in the asymmetric stretching vibration peak of $-CF_3$ from 1207.5 and 1184.9 cm^{-1} (in the case of PUL) to 1202.8 and 1182.3 cm^{-1} (in the case of PUL-TiO_{2-x}) strongly suggests an interaction between TiO_{2-x} and the $-CF_3$ moiety of the $TFSI^-$ anion [47, 48]. The interaction between TiO_{2-x} and $TFSI^-$ was further investigated through FTIR characterization. Figure 4(b) displays the FTIR spectra of PUL, PUL-TiO_2, and PUL-TiO_{2-x} in the 755–725 cm^{-1} range, which is relevant to the state of the $TFSI^-$ anion. Deconvolution of the spectra revealed two distinct Gaussian peaks, representing two dissociation states. The peak at 740 cm^{-1} corresponds to the S–N stretching bond of the free $TFSI^-$ anion, while the peak at 745 cm^{-1} originates from the bonded Li–TFSI ion pair [49, 50]. The proportion of free $TFSI^-$ anions in PUL-TiO_2 and PUL-TiO_{2-x} is significantly higher compared to PUL, indicating that the addition of inorganic fillers promotes the dissociation of the lithium salt. In contrast to PUL-TiO_2, PUL-TiO_{2-x} exhibits a marginal increase in the paired $TFSI^-$ anion content. This observation, in conjunction with the increased Li^+ transference number and ionic conductivity of PUL-TiO_{2-x}, suggests that the $TFSI^-$ anion is partially paired with the oxygen vacancies on the surface of TiO_{2-x}, rather than being paired with Li^+ ions. Based on the conducted characterization tests, as shown in Fig. 4(c), it was observed that TiO_{2-x} possesses the ability to adsorb $TFSI^-$ anions, leading to an increase in the Li^+ transference number. Additionally, we propose the existence of a Lewis acid-base interaction between TiO_{2-x} and ether oxygen groups. This interaction serves a dual purpose: firstly, it establishes a fast ion transport pathway at the organic/inorganic interface, thereby enhancing the ionic conductivity; secondly, it provides protection to the ether oxygen group and widens the electrochemical stability window of the electrolyte.

To investigate the interfacial stability of PUL-TiO_{2-x} with lithium metal and its inhibitory effect on lithium dendrite formation, a Li||Li symmetrical battery was assembled and tested at 40 °C. In the Tafel analysis (Fig. S8 in the ESM), the exchange current density of PUL-TiO_{2-x} (0.065 mA·cm^{-2}) is nearly three times that of PUL (0.022 mA·cm^{-2}), indicating that the addition of TiO_{2-x} significantly enhances charge transfer kinetics. As illustrated in Fig. 4(d), compared with Li|PUL|Li, Li|PUL-TiO_2|Li, and Li|PUL-TiO_{2-x}|Li symmetrical cells, the Li|PUL-TiO_{2-x}|Li cell delivered the lowest overpotential when charged/discharged from 0.1 to 1.0 mA·cm^{-2} with an areal capacity from 0.5 to 5.0 mAh·cm^{-2}. The Li|PUL-TiO_{2-x}|Li symmetric cell exhibited stable cycling for 1950 h, with a low overpotential of approximately 99.7 mV at a current density of 0.1 mA·cm^{-2} and a capacity of 0.1 mAh·cm^{-2} (Fig. 4(e)). In contrast,

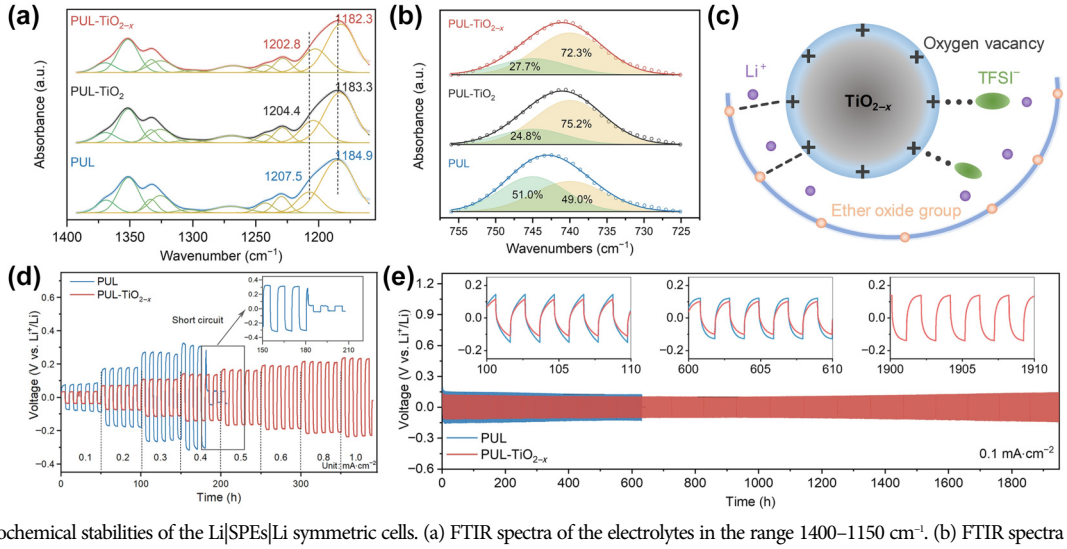

Figure 4 Electrochemical stabilities of the Li|SPEs|Li symmetric cells. (a) FTIR spectra of the electrolytes in the range 1400–1150 cm^{-1}. (b) FTIR spectra of the electrolytes in the range 755–725 cm^{-1}. (c) Prediction diagram of Lewis acid-base interaction between TiO_{2-x}, polymer, and lithium salt. (d) Rate capabilities of Li|SPEs|Li symmetric cells. (e) Voltage profiles for lithium plating/stripping experiment in a symmetric Li|SPEs|Li cell at current density of 0.1 mA·cm^{-2} for 0.1 mAh·cm^{-2}.

the Li|PUL|Li symmetric battery displayed an overpotential of around 126.5 mV. After 630 h of cycling, the voltage sharply dropped, indicating the puncturing of the electrolyte by lithium dendrite growth and resulting in a short circuit in the battery.

3.5 Evaluation of composite electrolyte performance in solid-state batteries

The electrochemical testing of the LFP|SPEs|Li cells are shown in Figs. 5(a) and 5(b). All cells were activated at 0.05 C in the incipient two cycles. The LFP|PUL-TiO_{2-x}|Li cell with a mass loading of 5 mg·cm^{-2} exhibits a high discharge capacity of 148 mAh·g^{-1} after 500 cycles at 0.3 C (1 C = 170 mA·g^{-1}). The corresponding capacity retention is 80.2% with an ultralow capacity decay of 0.04% per cycle, greatly higher than those of LFP|PUL-TiO_2|Li and LFP|PUL|Li cells. The cycling stability of the LFP|PUL-TiO_{2-x}|Li cell is far superior than the SPEs (paired with LFP cathodes) reported (Table S5 in the ESM). Due to the excellent ionic conductivity and low interfacial resistance, the capacities of the LFP|PUL-TiO_{2-x}|Li cells at 0.2, 0.3, 0.4, and 0.5 C are 170, 151, 133, and 118 mAh·g^{-1}, respectively (Fig. 5(c)). The electrochemical performance of PUL-TiO_{2-x} was further assessed through cyclic performance and rate performance tests of NCM811||Li solid-state batteries (1 C = 200 mA·g^{-1}). To enhance the interface contact between the solid electrolyte and the electrodes and mitigate interface impedance, a coating of the electrolyte was applied to the surface of the NCM811 positive electrode and the lithium metal negative electrode [51, 52], resulting in the fabrication of an integrated electrode (Fig. S9 in the ESM). This approach allowed the electrolyte to effectively fill the interparticle gaps within the electrodes and establish intimate contact with the lithium metal surface, thereby establishing a favorable pathway for ion transport.

Figure 5(d) depicts the rate performance of the NCM811||Li batteries at 40 °C within the voltage range of 3.0–4.3 V. At a lower rate of 0.2 C, the PUL-TiO_{2-x}, PUL-TiO_2, and PUL assembled batteries exhibited capacities of 172, 157, and 149 mAh·g^{-1}, respectively. However, as the current density increased, the discharge capacity of both batteries decreased. The PUL-TiO_2 and PUL electrolytes demonstrated relatively poor ion conductivity, resulting in a discharge specific capacity of only 100 and 87 mAh·g^{-1} at 0.5 C, respectively. Upon reverting to a current density of 0.2 C, the NCM811|PUL|Li and NCM811|PUL-TiO_2|Li cells exhibited a capacity of 150 and 122 mAh·g^{-1}, respectively. In contrast, benefiting from its high ionic conductivity and Li^+ transference number, the PUL-TiO_{2-x} electrolyte exhibited capacities of 172, 151, 133, and 118 mAh·g^{-1} at rates of 0.2, 0.3, 0.4, and 0.5 C, respectively. Even when the current density returned to 0.2 C, the battery's specific capacity remained at 163 mAh·g^{-1}, corresponding to 95.6% of the initial discharge capacity of 0.2 C. The solid-state battery assembled with PUL-TiO_{2-x} exhibited superior rate performance, demonstrating stability at high rates and delivering higher capacity. Figs. 5(e) and 5(f) presented the long-term cycling performance of the NCM811||Li battery at 40 °C and a rate of 0.2 C. After two activation cycles at a current density of 0.1 C, the NCM811|PUL|Li cell exhibited a discharge specific capacity of 153 mAh·g^{-1}, with a capacity retention rate of only 58.4% after 275 cycles. In contrast, the NCM811|PUL-TiO_{2-x}|Li battery displayed a higher discharge specific capacity of 171 mAh·g^{-1}, with a capacity retention rate of 75.1% after 275 cycles. Furthermore, the average coulombic efficiency of the NCM811|PUL-TiO_{2-x}|Li battery was 99.5%, indicating favorable capacity utilization and cycle stability. The cycling performance at a higher rate (0.5 C) is presented in Fig. S10 in the ESM. The cyclic voltammetry (CV) curves depicted in Fig.

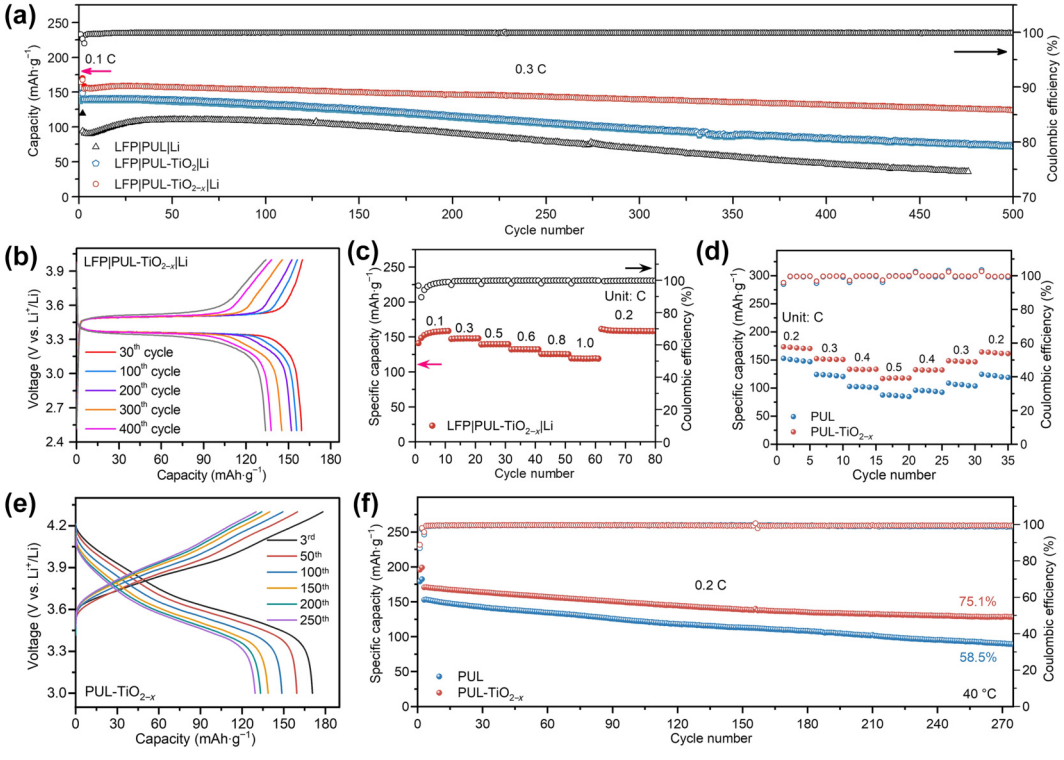

Figure 5 Electrochemical performances of solid-state batteries at 40 °C. ((a) and (b)) The cycling performances (a) and voltage profiles (b) of solid-state LFP|SPEs|Li cells cycled at 0.2 C. (c) Rate performances of solid-state LFP|PUL-TiO_{2-x}|Li cells. (d) Rate performances for PUL and PUL-TiO_{2-x} at 0.05–0.5 C. ((e) and (f)) The cycling performances (e) and voltage profiles (f) of solid-state NCM811|SPEs|Li cells cycled at 0.2 C.

S11 in the ESM reveal that in comparison to PUL, the batteries assembled with PUL-TiO_{2-x} exhibit clearer and more defined redox peaks, indicative of enhanced reversibility and accelerated kinetic rates. The larger peak areas observed further affirm the improvement in electrochemical activity and the acceleration of reaction rates. Furthermore, we further evaluated the stability between NCM811 and the electrolytes through electrochemical floating experiments. The results, as shown in Fig. S12 in the ESM, indicate that PUL-TiO_{2-x} maintains extremely low leakage currents under harsh constant voltage conditions of 4.3, 4.4, and 4.5 V. These improved performance characteristics can be attributed to the PUL-TiO_{2-x} composite electrolyte, which facilitates faster ion transport, effectively suppresses electrolyte decomposition, and ensures the stable operation of the battery throughout the cycling process.

4 Conclusion

In this work, we successfully synthesized PU via a linear stepwise addition polymerization reaction. The PU structure consists of alternating soft and hard segments, which exhibit favorable ion transfer capability and excellent mechanical properties. By incorporating dispersed nanofillers TiO_{2-x} into the PU matrix, we constructed a solid polymer electrolyte with high ionic conductivity and a wide electrochemical stability window. The incorporation of TiO_{2-x} effectively reduced the crystallinity of the polymer, thereby enhancing its amorphous nature. Moreover, the abundant Lewis acid sites on the surface of TiO_{2-x} interacted with the ether oxygen groups, leading to improved structural protection and the formation of efficient ion transport channels. As a result, significant enhancements were observed in both the electrochemical stability window (4.98 V) and ionic conductivity (2.19×10^{-4} S·cm^{-1} at 40 °C). Furthermore, the interaction between TiO_{2-x} and the $TFSI^-$ anion facilitated the release of a higher number of free lithium ions, contributing to an increased Li^+ transference number (0.47). The excellent ion transport characteristics and high voltage resistance of the solid electrolyte were further confirmed by the long-term cycling stability of the assembled NCM811||Li high-voltage batteries. Furthermore, PUL-TiO_{2-x} demonstrates extremely low capacity fade (0.04% per cycle) in LFP||Li batteries, confirming the universality of this electrolyte across different systems. Overall, this study provides valuable insights into the design and development of composite solid electrolytes for high-performance all-solid-state lithium-metal batteries.

Electronic Supplementary Material: Supplementary material (TEM, SEM, XRD, and ^{1}H NMR spectrum measurements) is available in the online version of this article at https://doi.org/10.26599/NR.2025.94907304.

Data availability

All data needed to support the conclusions in the paper are presented in the manuscript and the Electronic Supplementary Material. Additional data related to this paper may be requested from the corresponding author upon request.

Acknowledgements

This work was supported by the National Key R&D Program of China (No. 2023YFB2503804), the National Natural Science Foundation of China (No. 52202236), and China Postdoctoral Science Foundation (Nos. 2024T170300 and 2022M711232). The authors thank the Analytical and Testing Center of Huazhong University of Science and Technology (HUST) and State Key Laboratory of Materials Processing and Die & Mould Technology for characterizations.

Declaration of competing interest

All the contributing authors report no conflict of interests in this work.

Author contribution statement

X. N. X.: Data curation, validation, writing manuscript, experimental design. F. P.: Data curation, project administration, validation, experimental design. W. J. L., J. L., Y. H. Y., and H. H. X.: Data curation, validation. Z. L. and Y. H. H.: Project administration, funding acquisition, writing manuscript. All the authors have approved the final manuscript.

Use of AI statement

None.

References

[1] Li, M.; Lu, J.; Chen, Z. W.; Amine, K. 30 years of lithium-ion batteries. *Adv. Mater.* **2018**, *30*, 1800561.

[2] Huo, S. D.; Sheng, L.; Xue, W. D.; Wang, L.; Xu, H.; Zhang, H.; Su, B.; Lyu, M.; He, X. M. Challenges of stable ion pathways in cathode electrode for all-solid-state lithium batteries: A review. *Adv. Energy Mater.* **2023**, *13*, 2204343.

[3] Chen, J.; Wu, J. W.; Wang, X. D.; Zhou, A. A.; Yang, Z. L. Research progress and application prospect of solid-state electrolytes in commercial lithium-ion power batteries. *Energy Storage Mater.* **2021**, *35*, 70–87.

[4] Wu, F. X.; Maier, J.; Yu, Y. Guidelines and trends for next-generation rechargeable lithium and lithium-ion batteries. *Chem. Soc. Rev.* **2020**, *49*, 1569–1614.

[5] Wang, H.; An, H. W.; Shan, H. M.; Zhao, L.; Wang, J. J. Research progress on interfaces of all-solid-state batteries. *Acta Phys.-Chim. Sin.* **2021**, *37*, 2007070.

[6] Zhao, Q.; Stalin, S.; Zhao, C.Z.; Archer, L. A. Designing solid-state electrolytes for safe, energy-dense batteries. *Nat. Rev. Mater.* **2020**, *5*, 229–252.

[7] Wang, Z. F.; Zhao, J.; Zhang, X. D.; Rong, Z. Y.; Tang, Y. F.; Liu, X. Y.; Zhu, L. Y.; Zhang, L. Q.; Huang, J. Y. Tailoring lithium concentration in alloy anodes for long cycling and high areal capacity in sulfide-based all solid-state batteries. *eScience* **2023**, *3*, 100087.

[8] Ji, Y.; Wang, Z. F.; Zhao, C. T.; Fang, Z. Q.; Gong, Y.; Jing, Q. H.; Xia, Y.; Luan, T. J.; Jiang, Y. Y.; Liang, J. W. et al. Diffusion-free all-solid-state batteries enabled by an ionic/electronic dual-conductive anode. *Renewables* **2024**, *2*, 194–203.

[9] Wu, J. Y.; Yuan, L. X.; Zhang, W. X.; Li, Z.; Xie, X. L.; Huang, Y. H. Reducing the thickness of solid-state electrolyte membranes for high-energy lithium batteries. *Energy Environ. Sci.* **2021**, *14*, 12–36.

[10] Liu, F. F.; Zhang, Z. W.; Ye, S. F.; Yao, Y.; Yu, Y. Challenges and improvement strategies progress of lithium metal anode. *Acta Phys.-Chim. Sin.* **2021**, *37*, 2006021.

[11] Zhao, Y.; Wang, L.; Zhou, Y. N.; Liang, Z.; Tavajohi, N.; Li, B. H.; Li, T. Solid polymer electrolytes with high conductivity and transference number of Li ions for Li-based rechargeable batteries. *Adv. Sci.* **2021**, *8*, 2003675.

[12] Tang, C. K.; Yu, L. Y.; Jiang, Q. K.; Gu, R. M.; Zhang, Y. M.; Liu, Z. Q.; Cai, W. L.; Wu, H.; Zhang, Y.; Yao, M. Polymer-based electrolyte for lithium-based high-energy-density and safe energy storages devices: Strategy and mechanisms. *Renewables* **2024**, *2*, 297–340.

[13] Reinoso, D. M.; Frechero, M. A. Strategies for rational design of polymer-based solid electrolytes for advanced lithium energy storage applications. *Energy Storage Mater.* **2022**, *52*, 430–464.

[14] Meng, N.; Lian, F.; Cui, G. L. Macromolecular design of lithium conductive polymer as electrolyte for solid-state lithium batteries. *Small* **2021**, *17*, 2005762.

[15] Lin, Z. Y.; Guo, X. W.; Zhang, R.; Tang, M. X.; Ding, P. P.; Zhang, Z. H.; Wu, L. Q.; Wang, Y. T.; Zhao, S.; Zhang, Q. et al. Molecular structure adjustment enhanced anti-oxidation ability of polymer electrolyte for solid-state lithium metal battery. *Nano Energy* **2022**, *98*, 107330.

[16] Yang, L. X.; Luo, D.; Zheng, Y.; Yang, T. Z.; Ma, Q. Y.; Nie, Y. H.; Dou, H. Z.; Zhang, Y. G.; Huang, R.; Yu, A. P. et al. Heterogeneous nanodomain electrolytes for ultra-long-life all-solid-state lithium-metal batteries. *Adv. Funct. Mater.* **2022**, *32*, 2204778.

[17] Xu, S. J.; Sun, Z. H.; Sun, C. G.; Li, F.; Chen, K.; Zhang, Z. H.; Hou, G. J.; Cheng, H. M.; Li, F. Homogeneous and fast ion conduction of PEO-based solid-state electrolyte at low temperature. *Adv. Funct. Mater.* **2020**, *30*, 2007172.

[18] Huo, H. Y.; Wu, B.; Zhang, T.; Zheng, X. S.; Ge, L.; Xu, T. W.; Guo, X. X.; Sun, X. L. Anion-immobilized polymer electrolyte achieved by cationic metal–organic framework filler for dendrite-free solid-state batteries. *Energy Storage Mater.* **2019**, *18*, 59–67.

[19] Zhou, Q.; Ma, J.; Dong, S. M.; Li, X. F.; Cui, G. L. Intermolecular chemistry in solid polymer electrolytes for high-energy-density lithium batteries. *Adv. Mater.* **2019**, *31*, 1902029.

[20] Bae, J.; Li, Y. T.; Zhang, J.; Zhou, X. Y.; Zhao, F.; Shi, Y.; Goodenough, J. B.; Yu, G. H. A 3D nanostructured hydrogel-framework-derived high-performance composite polymer lithium-ion electrolyte. *Angew. Chem., Int. Ed.* **2018**, *57*, 2096–2100.

[21] Sun, Y. H.; Gao, M. D.; Li, H.; Xu, L.; Xue, Q.; Wang, X. R.; Bai, Y.; Wu, C. Application of metal–organic frameworks to the interface of lithium metal batteries. *Acta Phys.-Chim. Sin.* **2021**, *37*, 2007048.

[22] Xu, H. T.; Zhang, H. R.; Ma, J.; Xu, G. J.; Dong, T. T.; Chen, J. C.; Cui, G. L. Overcoming the challenges of 5 V spinel $LiNi_{0.5}Mn_{1.5}O_4$ cathodes with solid polymer electrolytes. *ACS Energy Lett.* **2019**, *4*, 2871–2886.

[23] Xi, G.; Xiao, M.; Wang, S. J.; Han, D. M.; Li, Y. N.; Meng, Y. Z. Polymer-based solid electrolytes: Material selection, design, and application. *Adv. Funct. Mater.* **2021**, *31*, 2007598.

[24] Zheng, F. F.; Li, C. W.; Li, Z. C.; Cao, X.; Luo, H. B.; Liang, J.; Zhao, X. D.; Kong, J. Advanced composite solid electrolytes for lithium batteries: Filler dimensional design and ion path optimization. *Small* **2023**, *19*, 2206355.

[25] Pei, F.; Huang, Y. M.; Wu, L.; Zhou, S. Y.; Kang, Q.; Lin, W. J.; Liao, Y. Q.; Zhang, Y.; Huang, K.; Shen, Y. et al. Multisite crosslinked poly(ether-urethane)-based polymer electrolytes for high-voltage solid-state lithium metal batteries. *Adv. Mater.* **2024**, *36*, 2409269.

[26] Liang, H. M.; Wang, L.; Wang, A. P.; Song, Y. Z.; Wu, Y. Z.; Yang, Y.; He, X. M. Tailoring practically accessible polymer/inorganic composite electrolytes for all-solid-state lithium metal batteries: A review. *Nano-Micro Lett.* **2023**, *15*, 42.

[27] Liu, S. L.; Liu, W. Y.; Ba, D. L.; Zhao, Y. Z.; Ye, Y. H.; Li, Y. Y.; Liu, J. P. Filler-integrated composite polymer electrolyte for solid-state lithium batteries. *Adv. Mater.* **2023**, *35*, 2110423.

[28] Pan, X. N.; Yang, P. X.; Guo, Y.; Zhao, K. J.; Xi, B. J.; Lin, F.; Xiong, S. L. Electrochemical and nanomechanical properties of TiO_2 ceramic filler Li-ion composite gel polymer electrolytes for Li metal batteries. *Adv. Mater. Interfaces* **2021**, *8*, 2100669.

[29] Banitaba, S. N.; Semnani, D.; Rezaei, B.; Ensafi, A. A. Evaluating the electrochemical properties of PEO-based nanofibrous electrolytes incorporated with TiO_2 nanofiller applicable in lithium-ion batteries. *Polym. Adv. Technol.* **2019**, *30*, 1234–1242.

[30] Qin, J. L.; Pei, F.; Wang, R.; Wu, L.; Han, Y.; Xiao, P.; Shen, Y.; Yuan, L. X.; Huang, Y. H.; Wang, D. L. Sulfur vacancies and 1T phase-rich MoS_2 nanosheets as an artificial solid electrolyte interphase for 400 $Wh{\cdot}kg^{-1}$ lithium metal batteries. *Adv. Mater.* **2024**, *36*, 2312773.

[31] Tang, S.; Guo, W.; Fu, Y. Z. Advances in composite polymer electrolytes for lithium batteries and beyond. *Adv. Energy Mater.* **2021**, *11*, 2000802.

[32] Mackanic, D. G.; Yan, X. Z.; Zhang, Q. H.; Matsuhisa, N.; Yu, Z. A.; Jiang, Y. W.; Manika, T.; Lopez, J.; Yan, H. P.; Liu, K. et al. Decoupling of mechanical properties and ionic conductivity in supramolecular lithium ion conductors. *Nat. Commun.* **2019**, *10*, 5384.

[33] Guo, Z. M.; Pang, Y. P.; Xia, S. X.; Xu, F.; Yang, J. H.; Sun, L. X.; Zheng, S. Y. Uniform and anisotropic solid electrolyte membrane enables superior solid-state Li metal batteries. *Adv. Sci.* **2021**, *8*, 2100899.

[34] Mackanic, D. G.; Michaels, W.; Lee, M.; Feng, D. W.; Lopez, J.; Qin, J.; Cui, Y.; Bao, Z. N. Crosslinked poly(tetrahydrofuran) as a loosely coordinating polymer electrolyte. *Adv. Energy Mater.* **2018**, *8*, 1800703.

[35] Dong, L. N.; Zeng, X. F.; Fu, J. F.; Chen, L. Y.; Zhou, J.; Dai, S. W.; Shi, L. Y. Cross-linked ionic copolymer solid electrolytes with loose coordination-assisted lithium transport for lithium batteries. *Chem. Eng. J.* **2021**, *423*, 130209.

[36] Huang, D. R.; Wu, L.; Kang, Q.; Shen, Z. Y.; Huang, Q. S.; Lin, W. J.; Pei, F.; Huang, Y. H. Amino-modified UiO-66-NH_2 reinforced polyurethane based polymer electrolytes for high-voltage solid-state lithium metal batteries. *Nano Res.* **2024**, *17*, 9662–9670.

[37] Pei, F.; Wu, L.; Zhang, Y.; Liao, Y. Q.; Kang, Q.; Han, Y.; Zhang, H. W.; Shen, Y.; Xu, H. H.; Li, Z. et al. Interfacial self-healing polymer electrolytes for long-cycle solid-state lithium-sulfur batteries. *Nat. Commun.* **2024**, *15*, 351.

[38] Wu, N.; Shi, Y. R.; Lang, S. Y.; Zhou, J. M.; Liang, J. Y.; Wang, W.; Tan, S. J.; Yin, Y. X.; Wen, R.; Guo, Y. G. Self-healable solid polymeric electrolytes for stable and flexible lithium metal batteries. *Angew. Chem., Int. Ed.* **2019**, *58*, 18146–18149.

[39] Wu, L.; Pei, F.; Cheng, D. M.; Zhang, Y.; Cheng, H.; Huang, K.; Yuan, L. X.; Li, Z.; Xu, H. H.; Huang, Y. H. Flame-retardant polyurethane-based solid-state polymer electrolytes enabled by covalent bonding for lithium metal batteries. *Adv. Funct. Mater.* **2024**, *34*, 2310084.

[40] Yao, Y.; Xu, Z. Y.; Liu, B.; Xiao, M.; Yang, J. H.; Liu, W. G. Multiple H-bonding chain extender-based ultrastiff thermoplastic polyurethanes with autonomous self-healability, solvent-free adhesiveness, and AIE fluorescence. *Adv. Funct. Mater.* **2021**, *31*, 2006944.

[41] Lai, Y.; Kuang, X.; Zhu, P.; Huang, M. M.; Dong, X.; Wang, D. J. Colorless, transparent, robust, and fast scratch-self-healing elastomers via a phase-locked dynamic bonds design. *Adv. Mater.* **2018**, *30*, 1802556.

[42] Cheng, C. Y.; Liu, H. Z.; Ouyang, C. Y.; Hu, N. G.; Zha, G.; Hou, H. Q. A high-temperature stable composite polyurethane separator coated Al_2O_3 particles for lithium ion battery. *Compos. Commun.* **2022**, *33*, 101217.

[43] Isfahani, A. P.; Sadeghi, M.; Nilouyal, S.; Huang, G. J.; Muchtar, A.; Ito, M. M.; Yamaguchi, D.; Sivaniah, E.; Ghalei, B. Tuning the morphology of segmented block copolymers with Zr-MOF nanoparticles for durable and efficient hydrocarbon separation membranes. *J. Mater. Chem. A* **2020**, *8*, 9382–9391.

[44] Li, Z.; Fu, J. L.; Zhou, X. Y.; Gui, S. W.; Wei, L.; Yang, H.; Li, H.; Guo, X. Ionic conduction in polymer-based solid electrolytes. *Adv. Sci.* **2023**, *10*, 2201718.

[45] Guo, Z. K.; Fan, L. S.; Zhao, C. Y.; Chen, A. S.; Liu, N. N.; Zhang, Y.; Zhang, N. Q. A dynamic and self-adapting interface coating for stable Zn-metal anodes. *Adv. Mater.* **2022**, *34*, 2105133.

[46] Yang, X. F.; Jiang, M.; Gao, X. J.; Bao, D. N.; Sun, Q.; Holmes, N.; Duan, H.; Mukherjee, S.; Adair, K.; Zhao, C. T. et al. Determining the limiting factor of the electrochemical stability window for PEO-based solid polymer electrolytes: Main chain or terminal–OH group. *Energy Environ. Sci.* **2020**, *13*, 1318–1325.

[47] Chen, H.; Adekoya, D.; Hencz, L.; Ma, J.; Chen, S.; Yan, C.; Zhao, H. J.; Cui, G. L.; Zhang, S. Q. Stable seamless interfaces and rapid ionic conductivity of Ca–CeO_2/LiTFSI/PEO composite electrolyte for high-rate and high-voltage all-solid-state battery. *Adv. Energy Mater.* **2020**, *10*, 2000049.

[48] Sun, Z. J.; Li, Y. H.; Zhang, S. Y.; Shi, L.; Wu, H.; Bu, H. T.; Ding, S. J. g-C_3N_4 nanosheets enhanced solid polymer electrolytes with excellent electrochemical performance, mechanical properties, and thermal stability. *J. Mater. Chem. A* **2019**, *7*, 11069–11076.

[49] Wu, N.; Chien, P. H.; Qian, Y. M.; Li, Y. T.; Xu, H. H.; Grundish, N. S.; Xu, B. Y.; Jin, H. B.; Hu, Y. Y.; Yu, G. H. et al. Enhanced surface interactions enable fast Li^+ conduction in oxide/polymer composite electrolyte. *Angew. Chem., Int. Ed.* **2020**, *59*, 4131–4137.

[50] Bakker, A.; Gejji, S.; Lindgren, J.; Hermansson, K.; Probst, M. M. Contact ion pair formation and ether oxygen coordination in the polymer electrolytes $M[N(CF_3SO_2)_2]_2PEO_n$ for M = Mg, Ca, Sr and Ba. *Polymer* **1995**, *36*, 4371–4378.

[51] Kang, Q.; Li, Y.; Zhuang, Z. C.; Wang, D. S.; Zhi, C. Y.; Jiang, P. K.; Huang, X. Y. Dielectric polymer based electrolytes for high-performance all-solid-state lithium metal batteries. *J. Energy Chem.* **2022**, *69*, 194–204.

[52] Zang Y.; Peng P.; Pei F.; Li, R. H.; Wu L.; Lu, D. Q.; Zhang Y.; Huang K.; Shen Y.; Huang Y. H. et al. Conjugated phthalocyanine based framework as artificial SEI for over 400 $Wh \cdot kg^{-1}$ lithium metal battery. *Natl. Sci. Rev.* **2024**, *12*, nwae443.